Journal of Controlled Release 354 (2023) 784–793

Contents lists available at ScienceDirect

Journal of Controlled Release

journal homepage: www.elsevier.com/locate/jconrel

Effect of Cellular and Microenvironmental Multidrug Resistance on Tumor-Targeted Drug Delivery in Triple-Negative Breast cancer

Okan Tezcan [a,b,*,1], Asmaa Said Elshafei [a,1], Karina Benderski [a,1], Elena Rama [a], Maike Wagner [a], Diana Moeckel [a], Robert Pola [c], Michal Pechar [c], Tomas Etrych [c], Saskia von Stillfried [d,e], Fabian Kiessling [a], Ralf Weiskirchen [f], Steffen Meurer [f], Twan Lammers [a,*]

[a] Department of Nanomedicine and Theranostics, Institute for Experimental Molecular Imaging, University Hospital RWTH Aachen, Aachen, Germany.
[b] UT Brown Foundation Institute of Molecular Medicine, UTHealth Houston, Houston, TX, USA
[c] Institute of Macromolecular Chemistry, Czech Academy of Science, Prague, Czech Republic
[d] Institute of Pathology, University Hospital RWTH Aachen, Aachen, Germany
[e] Center for Integrated Oncology Aachen Bonn Cologne Duesseldorf (CIO ABCD), University Hospital RWTH Aachen, Aachen, Germany
[f] Institute of Molecular Pathobiochemistry, Experimental Gene Therapy and Clinical Chemistry (IFMPEGKC), University Hospital RWTH Aachen, Aachen, Germany

ARTICLE INFO

Keywords:
Nanomedicine
Drug targeting
EPR effect
Tumor microenvironment
Multidrug resistance

ABSTRACT

Multidrug resistance (MDR) reduces the efficacy of chemotherapy. Besides inducing the expression of drug efflux pumps, chemotherapy treatment alters the composition of the tumor microenvironment (TME), thereby potentially limiting tumor-directed drug delivery. To study the impact of MDR signaling in cancer cells on TME remodeling and nanomedicine delivery, we generated multidrug-resistant 4T1 triple-negative breast cancer (TNBC) cells by exposing sensitive 4T1 cells to gradually increasing doxorubicin concentrations. In 2D and 3D cell cultures, resistant 4T1 cells are presented with a more mesenchymal phenotype and produced increased amounts of collagen. While sensitive and resistant 4T1 cells showed similar tumor growth kinetics in vivo, the TME of resistant tumors was enriched in collagen and fibronectin. Vascular perfusion was also significantly increased. Fluorophore-labeled polymeric (~10 nm) and liposomal (~100 nm) drug carriers were administered to mice with resistant and sensitive tumors. Their tumor accumulation and penetration were studied using multimodal and multiscale optical imaging. At the whole tumor level, polymers accumulate more efficiently in resistant than in sensitive tumors. For liposomes, the trend was similar, but the differences in tumor accumulation were insignificant. At the individual blood vessel level, both polymers and liposomes were less able to extravasate out of the vasculature and penetrate the interstitium in resistant tumors. In a final in vivo efficacy study, we observed a stronger inhibitory effect of cellular and microenvironmental MDR on liposomal doxorubicin performance than free doxorubicin. These results exemplify that besides classical cellular MDR, microenvironmental drug resistance features should be considered when aiming to target and treat multidrug-resistant tumors more efficiently.

1. Introduction

Chemotherapy is employed to treat many different types of malignancy and can induce partial or complete cancer regression. Beneficial initial responses are often followed by a relapse, as soon as cancer cells have developed multidrug resistance (MDR) [1]. At the cellular level, MDR can be mediated via cell cycle alterations, apoptosis inhibition, and increased activation of DNA damage repair mechanisms, as well as via overexpression of adenosine triphosphate-binding cassette (ABC) transporter proteins [2]. The latter plays a pivotal role in generalized MDR, as the exposure of cancer cells to a single agent, such as doxorubicin (dox), can result in development of cross-resistance to a broad range of similar and dissimilar chemotherapeutic compounds. ABC transporters, such as P-glycoprotein (Pgp), are ATP-powered small-molecule efflux pumps that maintain cellular homeostasis by pumping out toxins. Drug exposure-induced overexpression of these efflux pumps

* Corresponding authors.
E-mail addresses: okan.tezcan@uth.tmc.edu (O. Tezcan), tlammers@ukaachen.de (T. Lammers).
[1] These authors contributed equally to this work.

https://doi.org/10.1016/j.jconrel.2022.12.056
Received 26 October 2022; Received in revised form 21 December 2022; Accepted 28 December 2022
Available online 28 January 2023

reduces the intracellular levels of chemotherapeutic drugs, contributing to therapy resistance and disease relapse [3,4].

Standard chemotherapeutics are internalized via passively diffusing across the cell membrane, exposing them to Pgp and other efflux pumps [5,6]. Nanomedicine drugs, on the other hand, are internalized via endocytosis, bypassing membrane-anchored efflux pumps, and they eventually release their cargo in the perinuclear region within cancer cells [7]. What has remained underappreciated is that drug resistance is a complex phenomenon which occurs not only on the cellular level but also at the level of the tumor microenvironment (TME). At the TME level, not much is known about the impact of MDR on microenvironment remodeling and tumor-directed drug delivery.

During chemotherapy treatment and gradual MDR development, the TME has been shown to change and is associated with fibrosis development [8]. In normal tissues, physiological levels of fibrosis are beneficial for wound healing. Upon tissue damage, cytokines attract immune cells and induce fibroblast activation, leading to the deposition of extracellular matrix (ECM) material, mainly collagen [9]. In chemotherapy-treated cancerous tissues, the deregulated and continuous activation of these processes due to drug-induced cell death, altered cellular signaling and inflammation leads to ECM overproduction and fibrosis [10]. In this regard, a whole-genome expression analysis of resistant ovarian carcinoma cells indicated a link between MDR cancer cells and fibrosis, detecting a higher expression of genes encoding multiple ECM-related components, such as collagen type 1 (*Col1*), lysyl oxidase (*lox*), and transforming growth factor beta-1 (*Tgfb1*) [11]. In line with this, in ovarian cancer patients with poor chemotherapy responsiveness, a correlation between MDR induction and expression of ECM components was observed, including higher collagen type XI alpha 1 expression [12]. The deposition and (lox-mediated) crosslinking of connective tissue around cancer cells form a barrier that can prevent the accumulation and penetration of (nano)therapeutics in tumors. Furthermore, the accompanied increase in solid stress may lead to vascular compression and increase interstitial pressure, which would be deleterious for tumor-directed drug delivery.

We here studied the impact of cellular MDR on the composition of the TME and on tumor-directed drug delivery in the 4T1 triple-negative breast cancer (TNBC) mouse model. To support our rationale, we employed immunohistochemistry (IHC) to study surgical specimens from biobanked patient tumors, demonstrating that the ECM in TNBC lesions is indeed enriched in collagen upon multiple cycles of chemotherapy (Fig. 1a). In parallel, we generated multidrug-resistant 4T1 TNBC cells (4T1R) by treating sensitive cells (4T1S) with gradually increasing sublethal doses of dox for up to 60 passages and for more than one year (Fig. 1b-d). Using both cell types, we studied alterations in the expression levels of MDR- and epithelial-to-mesenchymal transition (EMT)-related genes and proteins via gene expression analysis, western blotting, IHC and fluorescence microscopy. Besides 2D cell culture, we

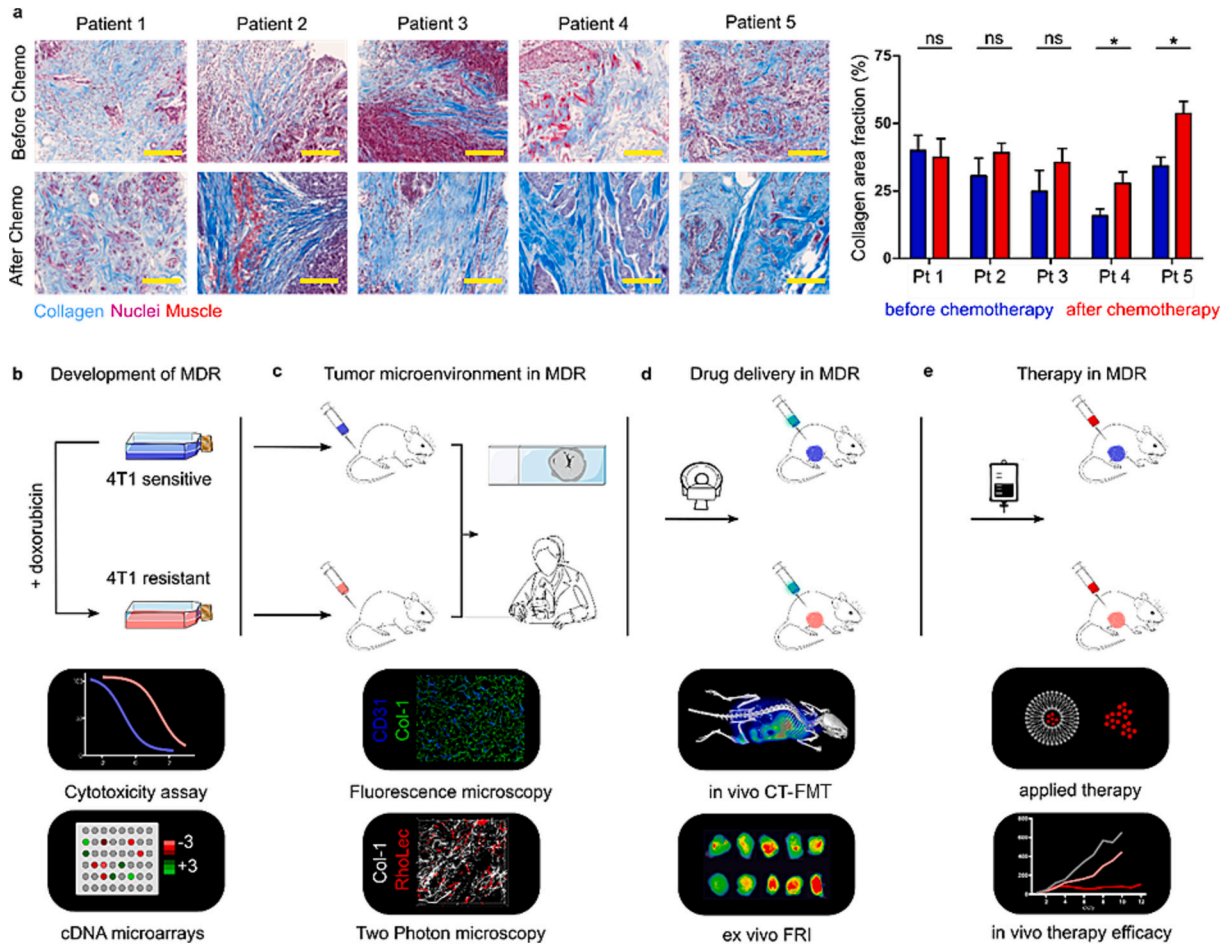

Fig. 1. Study motivation and setup. (a) Biobanked tumor tissue specimens of TNBC patients with poor chemotherapy outcomes were analyzed before and after neoadjuvant chemotherapy, showing that chemotherapy treatment results in enhanced collagen I deposition in the TME. (b) Our study setup initially involved the development of MDR 4T1 murine TNBC cells. MDR status was confirmed by cytotoxicity assays and microarray analysis. (c) Sensitive (4T1S) and resistant (4T1R) cells were inoculated into the mammary fat pad of Balb/c mice and a thorough analysis of the microenvironment was conducted using fluorescence microscopy and TPLSM. (d) The impact of MDR-induced microenvironmental changes on the accumulation and penetration of polymeric and liposomal nanocarriers was investigated using CT-FMT, FRI and TPLSM. (e) The effect of cellular and microenvironmental MDR on in vivo therapy outcomes was studied using free and liposomal dox. Scale bar = 50 μm.

also employed 3D homo- and heterospheroids (i.e., combined with NIH3T3 mouse fibroblasts) to assess ECM deposition (Fig. 1b). Next, 4T1S and 4T1R cells were inoculated orthotopically into the mammary fat pad of Balb/c mice, tumor growth kinetics were recorded and TME composition was analyzed using fluorescence and two-photon laser scanning microscopy (TPLSM) (Fig. 1c). Subsequently, using 3D in vivo computed tomography / fluorescence molecular tomography (CT-FMT), 2D ex vivo fluorescence reflectance imaging (2D FRI) and TPLSM, we investigated how the TME in sensitive versus resistant 4T1 tumors affects the accumulation and penetration of ~10 nm poly(*N*-(2-hydroxypropyl) methacrylamide) (pHPMA) polymers and ~ 100 nm pegylated liposomes (Fig. 1d). We finally studied the effect of cellular and microenvironmental MDR on in vivo treatment efficacy, using free and liposomal dox (Fig. 1e). Collectively, our results indicate that in the 4T1 murine TNBC model, MDR extends beyond the alterations at the cellular level, resulting in a TME with increased ECM abundance which affects nanodrug penetration and therapeutic efficacy.

2. Materials and methods

2.1. Cell lines

Dox-resistant 4T1 murine breast carcinoma cells (4T1R) were developed from chemotherapy-sensitive 4T1 cells (4T1S) by stepwise dose increments. Cells were cultivated in RPMI medium (Invitrogen, Germany), which was supplemented with 10% fetal calf serum (FCS; Invitrogen, Germany) and Penicillin/Streptomycin (Pen/Strep; Invitrogen, Germany). During resistant cell development, cells were frozen for long-term storage, thawed, and re-cultivated several times for the experiments. Cell passaging was performed in T75 cell culture flasks (Cell Star, Greiner, Germany) when the cell confluency reached approximately 80%. Cells were incubated at 37 °C with 5% CO_2 conditions. NIH3T3 fibroblasts (ATCC) were used for three-dimensional heterospheroid studies with the combination of 4T1S and 4T1R cells.

2.2. Chemotherapeutics

Doxorubicin (dox) hydrochloride (LC Laborites, USA) was used for creating 4T1R cells, for cytotoxicity analysis, and for in vivo therapy studies. Doxil (Janssen-Cilag International, Belgium) is a dox-loaded and pegylated liposome. Doxil efficacy was studied in 4T1S and 4T1R tumors. Dox and Doxil were intravenously injected into the tail vein of anesthetized mice at a dose of 5 mg/kg body weight.

2.3. Cytotoxicity analysis

Cytotoxicity was assessed using an XTT kit (PanReac AppliChem, Germany). Cells were seeded in 96 well plates and cultured overnight at 37 °C with 5% CO_2. Then, drugs were applied at 14 different concentrations for 72 h. The XTT reagent was applied, and the absorbance at 475 nm was recorded using a reference wavelength of 690 nm to detect cell viability. To evaluate the cytotoxicity of drugs (or any inhibitory substances), the inhibitory concentration 50 (IC_{50}) value is measured. This value indicates the dose of any particular substance which inhibits 50% of biological activity.

2.4. Cell migration assay

The Boyden chamber cell migration assay was performed to detect the migratory potential of 4T1S and 4T1R cells. Cells were harvested from the culture flasks with Trypsin/EDTA solution and washed three times with FCS-free RPMI culture media. Cells were then resuspended in an FCS-free RPMI medium. The cell suspension was added to the transwell membrane. The lower chamber was filled with RPMI culture medium supplemented with 20% FCS. The upper section was located on top of the lower chamber and incubated for 72 h at 37 °C with 5% CO_2. The non-migrated cells were scraped off with the help of a cotton swap two times. Then, the remaining cells were fixed with 100% methanol for 10 min. This was followed by DAPI staining for 5 min and washing steps with DPBS. Migrated cells were quantified through the area percentage of DAPI signal via Image J (National Institutes of Health, USA) using the images captured by fluorescence microscope at 5× magnification.

2.5. Microarray analysis

4T1S and 4T1R cells were subjected to microarray-based gene expression analysis. First, the total RNA of 4T1 cells was isolated using the RNeasy Mini Kit® (Qiagen, Germany). GeneChip® (Affymetrix, USA) analysis was performed according to the manufacturer's instructions. Up-and-down-regulated genes with at least 1.5-fold change compared to the control groups were classified according to their roles.

2.6. 3D tumor spheroid assay

The 3D tumor spheroid assay provides an in vitro platform to analyze cancer cell behavior and the interactions between cancer and stroma cells, such as myofibroblasts and macrophages. Sensitive and resistant 4T1 cells were subjected to the hanging drop 3D tumor spheroid technique to form homospheroids. Additionally, 4T1 cells were co-seeded with murine fibroblasts with different ratios (1:1 and 1:5; 4T1 cells and NIH3T3 fibroblasts, respectively) to form heterospheroids. Cells were prepared with 20 μl of cell suspension and seeded on a lid of 96 well plates. Cells were incubated for 72 h at 37 °C with 5% CO_2. After the incubation, the spheroids were transferred into the freezing chambers and frozen with Tissue-Tek (Sakura, Japan). Homo- and heterospheroids were cryosectioned and placed onto the microscope slides for further immunohistochemistry staining and microscopy analysis.

2.7. Western blot analysis

Proteins were collected from the lysates and supernatants of 4T1S and 4T1R cells and separated using denaturing and reducing conditions. Separated proteins were subjected to a Western blot and transferred onto a nitrocellulose membrane. Proteins of interest (Pgp, Col-I, Fibronectin (FN) and lox) were detected via specific antibody binding and chemiluminescence imaging. Beta-actin was used as a housekeeping protein for normalization and quantification.

2.8. Immunocytochemistry staining

Both sensitive and resistant cells were seeded onto round coverslips inserted in 24 well plates. After overnight incubation, cells were fixed with 4% paraformaldehyde (PFA) for 20 min and washed with DPBS. Primary antibodies were added, and cells were incubated for one hour for specific binding. After the washing steps, cells were subjected to secondary antibody staining for 30 min. The round coverslips were then transferred onto the microscope slides for microscopy analysis. Antibodies and dilutions used were: Primary: anti-Pgp (1:100) (Biozol, Germany), anti-Col-1 (1:100) (Novus Biologicals, Germany), Anti-FN (1:100) (abcam,UK), anti-Lox-1 (1:100) (Novus Biologicals, Germany), anti-Collagen IV (1:100) (Novotec, Germany), anti-CD31 (1:50) (BD Biosciences, USA), anti-α smooth muscle layer (αSMA) (1:100) (Progen, Germany), anti-vascular endothelial growth factor receptor 2 (VEGFR2) (1:20) (R&D Systems,USA). Secondary: Alexa Fluor 488 anti-Rabbit (1:500), AMCA anti-Rabbit (1:50), Alexa Fluor 488 anti-Rat (1:350), AMCA anti-Goat (1:50), AMCA (blue) anti-Biotin (1:200) (Dianova, Germany), DAPI (1:500) (Merck, Germany).

2.9. Fluorophore-labeled nanoparticles

pHPMA was used as a small-sized nanocarrier. The polymer used had a molecular weight of 67 kDa, corresponding to a size of 10–20 nm, and

a polydispersity of 1.7 [13]. Two fluorescent dyes were conjugated to pHPMA, at a concentration of 2.5 wt-% (generating pHPMA-ATTO488 and pHPMA-Dy750). Pegylated liposomes were prepared as described in [14]. They were 100 nm in size and labeled with two different dyes, via incorporating Cy7-DSPE and BDP-DSPE.

2.10. Mouse model

Animal protocols were approved by the German State Office for Nature, Environment and Consumer Protection (LANUV) North Rhine-Westphalia. Six to nine-week-old Balb/c female mice were purchased from Janvier Labs (Le Genest-Saint-Isle, France) and housed in a specific pathogen-free environment, under 12 h light/dark cycles and at a temperature of 21–23 °C, with a relative humidity of 35–65%. After 7 days of acclimation, mice were initiated on tumor injection under anesthesia. Mice were randomly assigned to the respective groups, with 5 mice per group. Mice were fed a chlorophyll-free diet (Ssniff, E15051) to avoid background fluorescence in the gastrointestinal tract during in vivo FMT and ex vivo FRI scans. The body weight and condition of the animals were observed daily. At the time of sacrifice, mice were anesthetized using isoflurane, followed by cervical dislocation and organ removal.

2.11. In vivo and ex vivo imaging

To evaluate the nanoparticle accumulation and distribution, fluorophore-labeled pHPMA polymers (~10 nm) and pegylated liposomes (~100 nm) were i.v. administered. Mice were scanned under inhalation anesthesia with 3D μCT-FMT (MILabs e.V., The Netherlands) at 0.25 h, 4 h, 24 h, 48 h, and 72 h after nanocarrier injection. Then, mice were injected with rhodamine-lectin (*Ricinus Communis* Agglutinin I Rhodamine, Vector Laboratories, USA) to visualize functional blood vessels. Subsequently, mice were sacrificed, and tumors and healthy organs were harvested for scanning via 2D FRI to monitor the biodistribution of fluorophore-labeled nanocarriers. 2D FRI and 3D μCT-FMT images were analyzed using Imalytics Preclinical Software 3.0 (Gremse- IT, Germany).

2.12. Immunohistochemistry staining

Paraffin blocks of human tissues were cut to 5 μm thick with a microtome. Antigen retrieval was performed at 60 °C for 2 h. followed by tissue deparaffinization using xylol and ethanol serial dilution for 1 h. Then, Masson's trichrome staining (Abcam, Berlin, Germany) was performed. Finally, the stained sections were mounted with vitrocloud to allow the coverslip to attach to the sample. Overviews and 20× images of stained tissues were acquired using Vectra 3.0 Microscope Automated Quantitative Pathology Imaging. Frozen mouse tumor tissue was cryosectioned as 8 μm thick slices and stained for different markers using specific primary and secondary antibodies. The immunohistochemistry protocol included a pre-washing step with DPBS for 2 min and fixing with 80% methanol for 5 min and with acetone for 2 min. The primary antibodies were applied, and samples were incubated for 1 h at room temperature. This was followed by triplicate washing to eliminate unbound antibodies. Then, secondary antibodies were applied for 30 min, at room temperature. Washing steps with DPBS were again applied after secondary antibody staining. Finally, slices were covered by a coverslip using Mowiol for embedding and stored at 4 °C for further fluorescence microscopy analysis.

2.13. Fluorescence microscopy

A Zeiss® Axio imager M2 fluorescence microscope (Carl-Zeiss Microscopy GmbH, Germany) was used for in vitro and ex vivo evaluation. Protein expression level and intracellular drug accumulation studies were performed to validate the MDR phenotype of the cells. Tumor blocks were cryosectioned as 8 μm thick slices and stained, according to the immunohistochemistry staining protocols, for different markers to characterize the tumor microenvironmental features. Further penetration and distribution of fluorophore-labeled nanocarriers were visualized with fluorescence microscopy and images were processed using Definiens® Developer XD 2.0.4 (Germany). Briefly, Definiens rule sets drew concentric rings of different step sizes (up to 60 μm from the blood vessels) around the tumor blood vessels, and in each ring fluorescence intensity values of the accumulated fluorophore-labeled polymers or liposomes were obtained. From these values, the % distribution of polymers and liposomes was graphically plotted.

2.14. Two-photon laser scanning microscopy

Tumor slices were cryosectioned at 100 μm thickness for two-photon laser scanning microscopy (TPLSM; FV1000MPE Multiphoton Microscopy System, Olympus, Germany). Via this technique, fluorophore-labeled nanocarriers and rhodamine lectin-perfused blood vessels were visualized using a 25× water-immersed objective. Collagen fibers were monitored via second harmonic generation imaging. 50 *Z*-stacks, with the dimension of 500 μm × 500 μm × 50 μm, were obtained. Images were captured randomly from the tumor slices, and the fluorescence signal was obtained through the photo-multiplier tubes adjusted for the optimal emission spectra. TPLSM images were analyzed using the Imaris Software version 7.4 (Bitplane AG, Switzerland). The collagen fiber thickness and spacing were calculated using the trabeculat thickness feature of the BoneJ plugin in the image processing package Fiji [15,16].

2.15. Statistical analysis

Data are presented as means ± SEM. Statistical differences among groups were analyzed via an unpaired two-tailed Student's *t*-test or one-way ANOVA. p values <0.05 were considered to represent significant differences. All statistical analyses were performed using GraphPad Prism 9.0 (San Diego, CA, USA).

3. Results and discussion

3.1. Establishment of multidrug-resistant 4T1 cells

We set out to study how cellular MDR affects the composition of the TME and tumor-directed drug delivery. To this end, we generated a TNBC model reflecting the evolution of acquired drug resistance. We used 4T1 murine mammary cancer cells as the most frequently used TNBC mouse model, and doxorubicin (dox) as one of the most widely used chemotherapeutic drug [17,18]. We developed resistant 4T1 cells by gradually increasing dox concentrations in the cell culture media (Fig. 2a). During the process, 4T1 cells with increasing levels of resistance were obtained (4T1R20, 4T1R40, 4T1R60; Suppl. Fig. 1 a-c).

Cytotoxicity analysis confirmed gradual dox resistance (Suppl. Fig. 1 d-f). For sensitive (4T1S) and resistant (4T1R) cells, IC_{50} values (i.e., the drug concentration needed to induce 50% cell death) and resistance indices were calculated. The IC_{50} value for dox in 4T1R cells was found to be significantly higher than in 4T1S cells, as evidenced by an almost 50-fold increase (Fig. 2b and c). Cells treated only with dox developed cross-resistance to paclitaxel (Fig. 2d and e; Suppl. Fig. 1 g-i). Conversely, no cross-resistance to cisplatin was observed (Suppl. Fig. 1 j-l), in line with the notion that cisplatin is not a Pgp substrate [19].

While MDR is multifactorial, it is mainly associated with the overexpression of Pgp [20–22]. We assessed Pgp levels via Western blot and immunofluorescence microscopy, demonstrating significantly higher expression of Pgp in 4T1R than in 4T1S cells (Fig. 2f-i). As expected, the highest level of Pgp expression was detected in the 4T1R60 cells, which had the highest level of dox resistance (Suppl. Fig. 1a-c). These findings are consistent with previous reports that drug resistance is proportional to the level of Pgp expression [23,24]. We validated Pgp efflux functionality using dox as a fluorescent probe. Following incubation, 4T1S

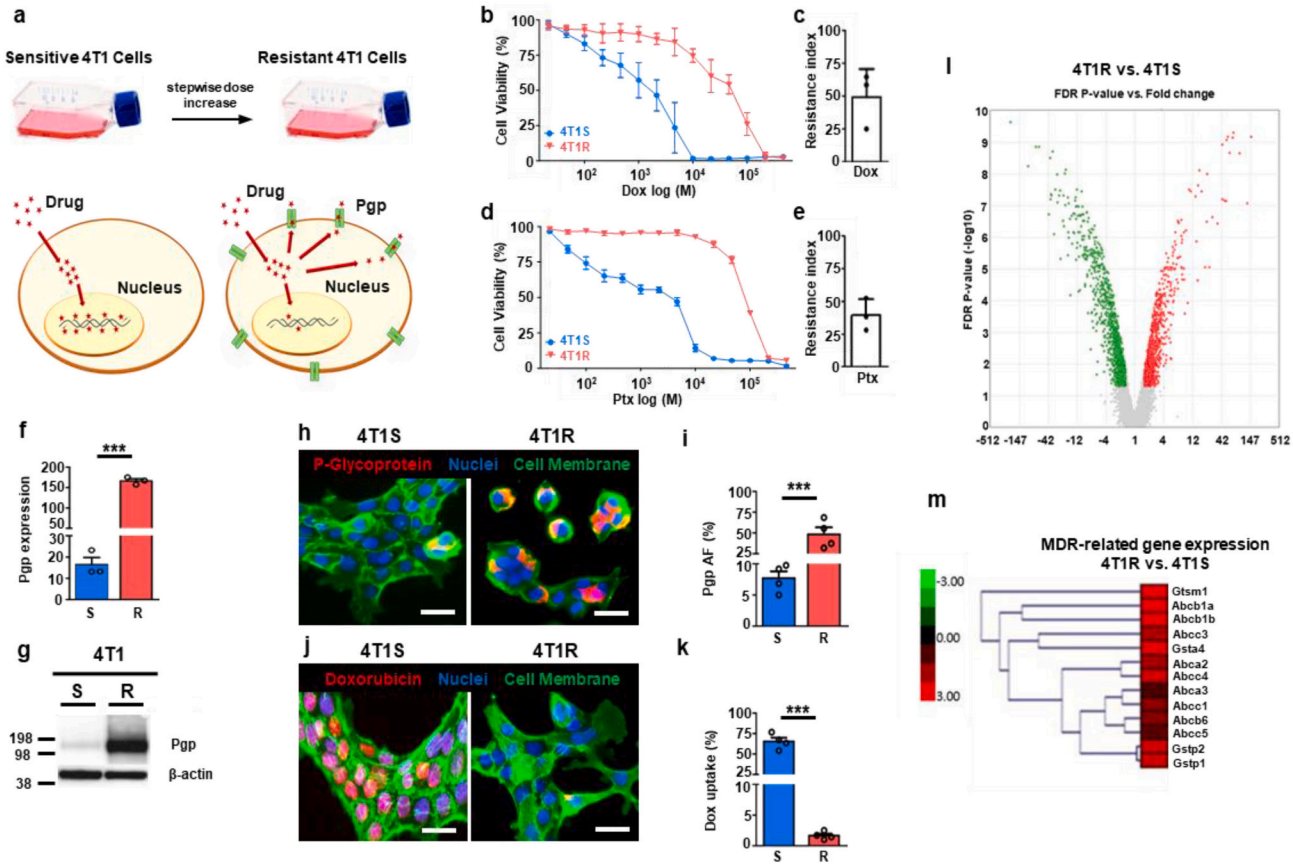

Fig. 2. Establishment of multidrug-resistant 4T1 cells. (a) Multidrug-resistant 4T1 cells were generated by exposure to gradually increasing concentrations of dox. (b-c) Cell viability and resistance index analysis show significant dox resistance development. (d-e) Cell viability and resistance index analysis of dox-resistant 4T1R cells demonstrate cross-resistance to paclitaxel. (f-g) Western blot quantification of Pgp expression reveals a significantly higher level of Pgp in 4T1R vs. 4T1S cells. (h-i) Fluorescence microscopy images and quantification confirm the overexpression of Pgp (red) in 4T1R cells. (j-k) Fluorescence microscopy images and quantification of dox (red) uptake in 4T1S and 4T1R cells. Significantly higher dox fluorescence was observed in the nuclei of 4T1S as compared to 4T1R cells. (l) Results of cDNA microarray analysis, showing that multiple genes were differentially regulated in 4T1S vs. 4T1R cells. (m) Upregulation of MDR-related genes in 4T1R vs. 4T1S cells, as assessed using microarray analysis. Scale bar = 50 μm. *** $p < 0.0001$. (For interpretation of the references to colour in this figure legend, the reader is referred to the web version of this article.)

cells displayed an intense fluorescence signal in the nuclei, while this was barely detectable in 4T1R cells (Fig. 2j-k). Flow cytometry analysis confirmed that with gradual MDR development, cells showed decreasing levels of intracellular dox (Suppl. Fig. 1 m-q). Multiple strategies have been explored to overcome cancer cell drug resistance [25,26]. For Pgp, several inhibitors have been developed, including tariquidar. By using tariquidar in in vitro cytotoxicity experiments, we were able to demonstrate that the dox resistance induced in 4T1R cells is specifically mediated by Pgp (Suppl. Fig. 2).

Gene expression profiles of 4T1S and 4T1R cells were examined using cDNA microarrays. We found that many genes were differentially regulated in 4T1S versus 4T1R cells, belonging to various functional families involved in biological processes such as cell cycle, apoptosis, adhesion, EMT and MDR (Fig. 2l). In line with the observed MDR phenotype, more than a dozen ABC transporter-related genes were found to be upregulated in 4T1R cells (Fig. 2m). Collectively, these results convincingly confirm the development of MDR in 4T1R cells upon prolonged exposure to increasing concentrations of dox.

3.2. Resistant cells undergo EMT and show increased collagen production

Several studies have demonstrated that cells treated with chemotherapeutics undergo EMT, which has been associated with the emergence of MDR [27–30]. For instance, Li *et al.* reported altered gene expression of EMT signature markers, i.e., vimentin upregulation and E-cadherin downregulation, in dox-treated MCF7 cells [30]. They also showed that dox treatment increased Pgp expression and decreased drug response, driving towards acquisition of MDR. During EMT, stationary epithelial cells were transformed into mobile mesenchymal cells, and these cells were shown to exhibit increased levels of migration and invasion. Also important to note is that mesenchymal cells, in particular cancer-associated fibroblasts, produce high amounts of fibrillar collagen and other ECM components, and thereby prominently contribute to fibrosis [31,32].

Bearing these notions in mind, we studied EMT-like features in 4T1S vs. 4T1R cells. Expression analysis showed that 17 genes associated with EMT were differentially regulated in 4T1R vs. 4T1S cells (Fig. 3a). Epithelial markers, such as keratins (Krt 7, 8, 14, 18, 19, and 80), epithelial cell adhesion molecule (Epcam), and cadherin 1 (Cdh1; encoding for E-cadherin) were downregulated. Vice versa, an upregulation of mesenchymal markers, such as vimentin (vim) and lox like-3 and 4 was observed (Fig. 3a). Fluorescence microscopy confirmed an increase in the expression of the EMT markers vim and lox in 4T1R vs. 4T1S cells (Fig. 3b-e). E-cadherin expression was expectedly downregulated in 4T1R cells compared to 4T1S cells (Fig. 3f and g). The motility of 4T1R cells was tested with the Boyden Chamber cell migration assay, which revealed that 4T1R cells were more migratory than 4T1S cells, in line with the acquired more mesenchymal phenotype (Fig. 3h and i). These notions are in line with our rationale and experimental setup, as EMT has been implicated in drug resistance in a variety of cancers, including pancreatic cancer [33], colorectal cancer [34],

breast cancer [35,36] and ovarian cancer [37].

Because cells undergoing EMT contribute to collagen synthesis in processes such as wound healing [38,39], we next investigated whether the more mesenchymal 4T1R cells produce more collagen as compared to the more epithelial 4T1S cells. To this end, we collected the supernatants from 4T1S and 4T1R cells and subjected the corresponding proteins to Western blot analysis using a Col-1 specific antibody (Fig. 3j). Our results show that 4T1R cells produce significantly more Col-1 than 4T1S cells (Fig. 3k). We validated these results in 3D tumor spheroids comprised exclusively of cancer cells (homospheroids; Fig. 3l) or mixtures of cancer cells and fibroblasts (heterospheroids; Fig. 3m). Fluorescence microscopy uncovered significantly higher Col-1 deposition in 4T1R vs. 4T1S homospheroids (Fig. 3n and p). Similarly, when co-cultured with NIH3T3 fibroblasts at two different cell ratios, higher Col-1 levels were detected in 4T1R vs. 4T1S heterospheroids (Fig. 3o and r). We conclude that in the 4T1 murine TNBC model, MDR is associated with EMT and expression and formation of ECM. This is in line with a previous report showing that lung cancer cells that have undergone EMT had increased expression of multiple ECM-related genes and also an increased collagen density in their TME [40]. Our results thus indicate that 4T1 murine TNBC cells influence their microenvironment via acquiring a more mesenchymal phenotype and via secretion of increased amounts of collagen.

3.3. Resistant 4T1 cells exhibit an altered tumor microenvironment

We next studied the in vivo tumor microenvironment upon induction of multidrug resistance via orthotopically inoculating 4T1S and 4T1R cells into the mammary fat pad of immunocompetent Balb/c mice (Fig. 4a). Tumor growth curves were recorded via caliper measurements and revealed no discernible difference between the growth kinetics of 4T1S and 4T1R tumors (Fig. 4b). Once tumor volumes reached the ethically allowed maximum volume, mice were injected with lectin (to study vascular perfusion) and sacrificed. Tumors were removed and cryosectioned for IHC and fluorescence microscopy examination.

As expected, Pgp expression was found to be significantly increased in 4T1R tumors (Fig. 4c and d). In line with the spheroid results, analysis of ECM components revealed a considerable increase in Col-1 and FN in

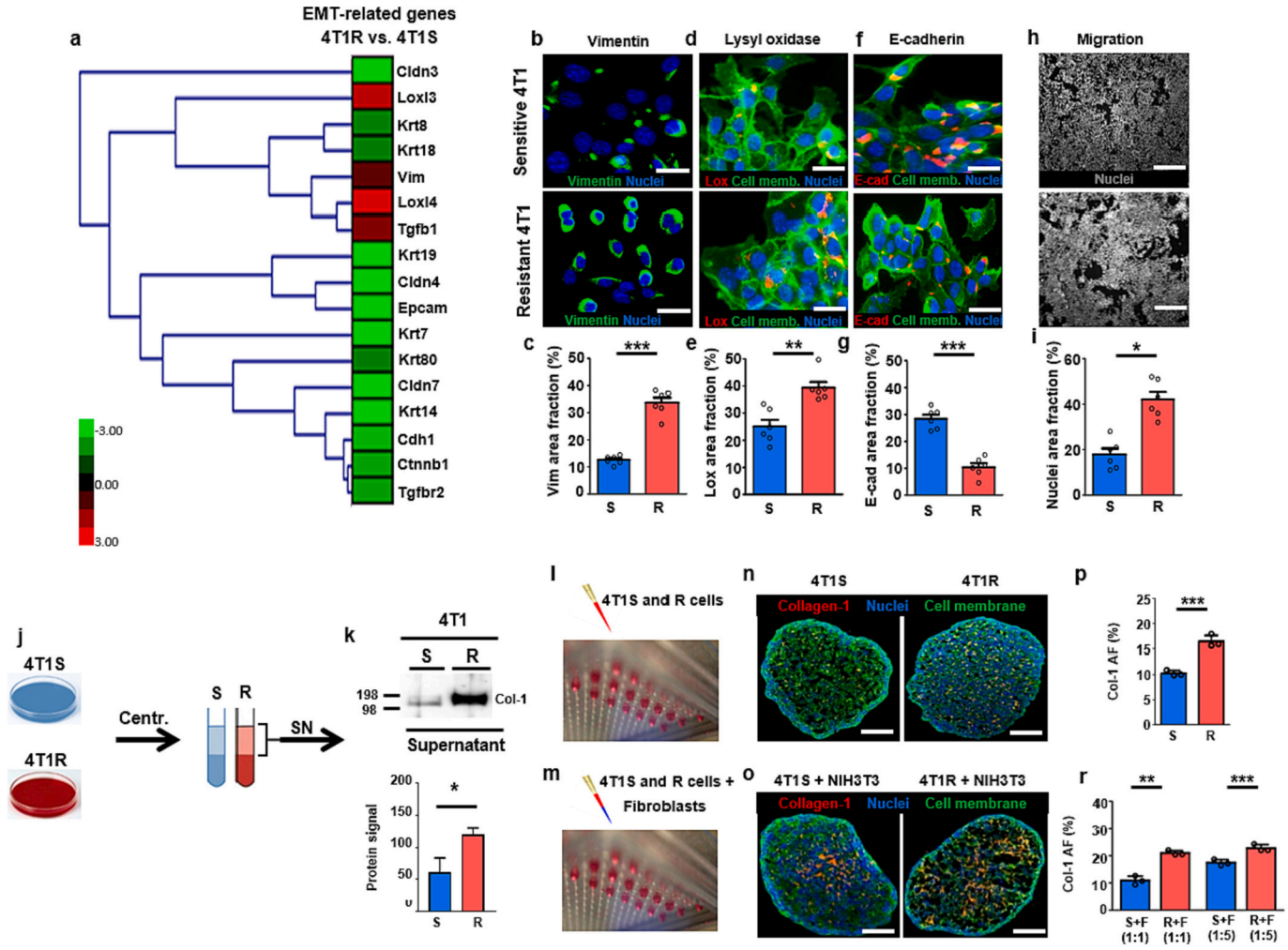

Fig. 3. Resistant 4T1 cells undergo EMT and produce increased amounts of collagen. (a) Heat map analysis of EMT -related genes reveals downregulation of markers related to an epithelial phenotype and upregulation of markers related to a mesenchymal phenotype in 4T1R cells. Fluorescence microscopy images and quantification showing significantly increased expression of the mesenchymal phenotype-associated proteins vim (green; b-c) and lox (red; d-e) and reduced expression of epithelial protein E-cadherin (red;f-g) in 4T1R cells. (h-i) Boyden chamber cell migration assay shows that mesenchymal-like 4T1R cells are significantly more migratory than epithelial-like 4T1S cells. (j-k) Western blot analysis and quantification show a higher amount of Col-1 in the supernatant of 4T1R cells vs. 4T1S cells. (l-r) Preparation of homo- and heterospheroids (co-cultured with NIH3T3 mouse fibroblast) through the 3D hanging drop culturing technique. Fluorescence microscopy images and quantification of spheroids stained for Col-1 (red) show that 4T1R cells deposit increased amounts of Col-1 in both homospheroids (n-p) and heterospheroids (o-r). For the latter, different cancer cell to fibroblast ratios was evaluated. These results show that MDR induction in 4T1 cells promotes EMT and collagen secretion. Scale bar = 50 μm. * $p < 0.05$, ** $p < 0.001$, *** $p < 0.0001$. (For interpretation of the references to colour in this figure legend, the reader is referred to the web version of this article.)

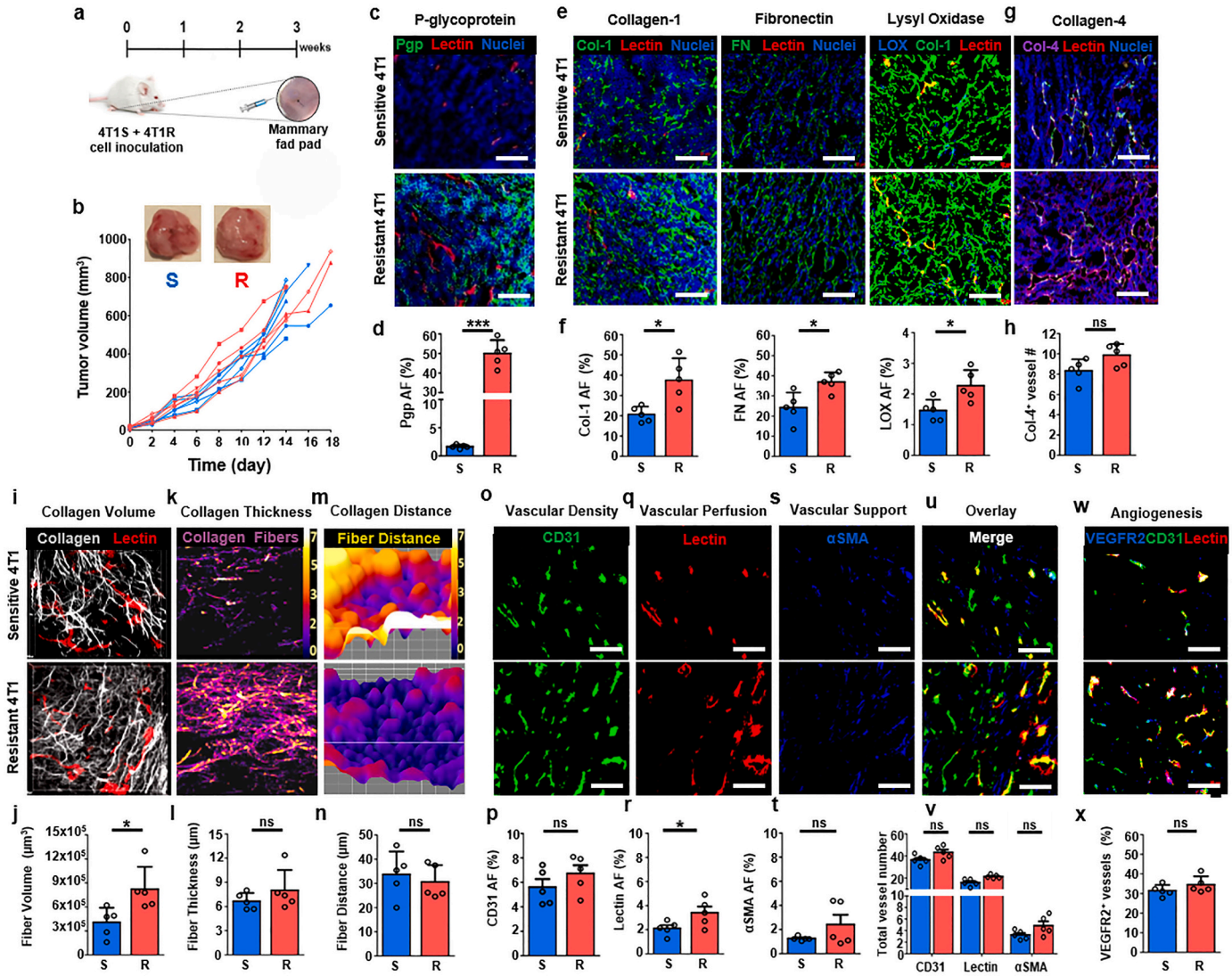

Fig. 4. MDR affects the microenvironment of 4T1 tumors. (a) Sensitive and resistant 4T1 cells were inoculated orthotopically into the mammary fat pad of Balb/c mice and tumors were harvested after 2–3 weeks. (b) Tumor growth curves show no difference between 4T1S and 4T1R cells. (c-d) Fluorescence microscopy imaging and quantification of Pgp expression, showing significantly higher expression in 4T1R tumors. (e-f) Microscopy imaging and quantification of ECM components, exemplifying that Col-1, lox and FN are overexpressed in 4T1R vs. 4T1S tumors. (g-h) Microscopy imaging and quantification showing identical collagen-4 expression in 4T1R and 4T1S tumors. (i-n) Two-photon laser scanning microscopy images exemplifying (via second harmonic generation imaging (a significantly higher total collagen volume density in 4T1R tumors, while collagen fiber thickness and the distance between individual collagen fibers were similar. (o-v) Fluorescence microscopy imaging and quantification of vessel density (CD31; o-p), vessel perfusion (lectin; q-r), vessel support (αSMA; s-t) and colocalization, indicating perfused, mature vessels (u-v). (w-x) Analysis of VEGFR2 expression in 4T1S and 4T1R tumors. Results plotted as the average of 4–5 representative images for $n = 5$ mice per group. Scale bar = 50 μm. * $p < 0.05$, *** $p < 0.0001$.

4T1R tumors compared to 4T1S tumors (Fig. 4e and f). The expression of the collagen-crosslinking enzyme lox-1 was also increased, while no difference was observed for basement membrane-associated collagen-4 (Fig. 4g and h). The results of immunohistochemistry were validated with western blots (Suppl. Fig. 3). Our results are in line with analyses performed in tumor tissue specimens obtained from TNBC patients before and after neoadjuvant chemotherapy (Fig. 1a), as well as with the findings of Echeverria et al., who reported the remodeling impact of chemotherapeutic treatment on TME of TNBC [41]. In their study, they showed that the microenvironment in dox and cyclophosphamide-unresponsive TNBC patient-derived xenografts (PDXs) had a denser ECM compared to pre-treatment biopsy specimens. As a noteworthy extension, our work shows that TME remodeling and ECM-richness not only result from exposing pre-existing tumors to chemotherapeutics but can already be triggered by inducing resistance (and MDR signaling) in cancer cells prior to inoculation and in vivo tumor formation.

The 3D collagen network in sensitive and resistant 4T1 tumors was further investigated by TPLSM, employing second harmonic generation imaging to visualize collagen fibers. The total volume of collagen fibers in 4T1R tumors was considerably higher than in 4T1S tumors (Fig. 4i and j). No significant differences in collagen fiber thickness (Fig. 4k and l) and collagen fiber distance (Fig. 4m and n) were observed between 4T1S and 4T1R tumors.

The tumor vasculature was examined via immunofluorescence microscopy of CD31, lectin, and αSMA. Vascular density as quantified by vascular area fraction was comparable between 4T1S and 4T1R tumors ($p = 0.44$) (Fig. 4o and p). Analysis of the perfused vessels (lectin positive area fraction) and vascular support (αSMA) indicated significantly higher and higher values for 4T1R tumors, respectively ($p = 0.043$ and $p = 0.28$, respectively; Fig. 4q-t). We finally also visualized and quantified the expression of VEGFR2 as a readout for angiogenesis, but did not observe a difference in 4T1S vs. 4T1R tumors (Fig. 4w and x). Together,

these results show that induction of MDR prior to tumor cell inoculation results in tumors with an altered ECM, with more collagen, and with a higher level of lox-mediated/collagen-crosslinking. Blood vessel density, functionality and pericyte support appeared to be somewhat increased, but were not significantly different. Altogether, it is shown that in the 4T1 murine TNBC model, induction of cellular MDR modulates the development of the TME.

3.4. Nanocarrier accumulation and penetration in resistant vs. sensitive 4T1 tumors

To evaluate the effect of the altered TME composition in 4T1R vs. 4T1S tumors on drug delivery, fluorophore-labeled pHPMA polymers (10 nm) and pegylated liposomes (100 nm) were i.v. injected into tumor-bearing mice. Hybrid μCT-FMT imaging was used to monitor the biodistribution and tumor accumulation of the nanocarriers. When studying whole-body biodistribution, tumor accumulation in both the 4T1R and 4T1S models were found to be very prominent for both polymers and liposomes (Suppl. Fig. 4). In vivo μCT-FMT analysis showed a higher accumulation of 10 nm pHPMA polymers in 4T1R vs. 4T1S tumors at 72 h after i.v. administration (Fig. 5a and c). This result was confirmed by ex vivo FRI (Fig. 5b and d), and can likely be explained by the observed increase in perfused vessels in 4T1R tumors. For 100 nm pegylated liposome accumulation, μCT-FMT results showed a trend but no significant increase in in vivo tumor accumulation in 4T1R vs. 4T1S tumors (Fig. 5e and g). Ex vivo, however, we again noticed higher liposome levels in 4T1R vs. 4T1S tumors (Fig. 5f and h).

Fluorescence microscopy and TPLSM were used to investigate the penetration of polymeric and liposomal drug delivery systems from blood vessels into the interstitium in 4T1S and 4T1R tumors. Fig. 5i-p show representative 2D and 3D microscopy images of fluorophore-labeled polymers and liposomes penetrating into and distributing across the tumor interstitium. A script for the program Definiens® Developer XD 2.0.4 was employed to quantify the levels of nanocarrier penetration and distribution from the vessel compartment into deeper tumor interstitial compartments (Fig. 5k and o). In both 4T1S and 4T1R tumors, the highest level of polymer and liposome localization was observed in the *peri*-vascular region, i.e., in the first 0–20 μm away from the tumor blood vessel wall. Importantly, however, in line with significantly increased levels of collagen deposition and ECM-richness in 4T1R cells in vitro (Fig. 3), in 4T1R tumors in vivo (Fig. 4) and in chemotherapy-treated TNBC patients (Fig. 1a), we noted a clear reduction in nanocarrier penetration from the vascular compartment into the interstitium in 4T1R vs. 4T1S tumors (Fig. 5l and p). Accordingly, in the deepest tumor compartments (i.e., 40–60 μm away from the blood vessel wall), the lower levels of polymeric and liposomal nanocarriers were detected in 4T1R tumors (albeit only significant for polymers). These findings exemplify the deleterious impact of stromal enrichment induced by MDR on nanomedicine penetration and distribution in tumors.

3.5. Nanomedicine treatment efficacy in sensitive vs. resistant 4T1 tumors

To evaluate the impact of MDR-induced microenvironmental changes on therapeutic efficacy, we intravenously administered free dox and pegylated liposomal dox (Doxil) to 4T1S and 4T1R tumor-bearing mice. Dox and Doxil treatment were carried out twice weekly for three weeks (Fig. 6a). In line with previous results (Fig. 4b), tumor growth showed no significant difference between untreated 4T1S and

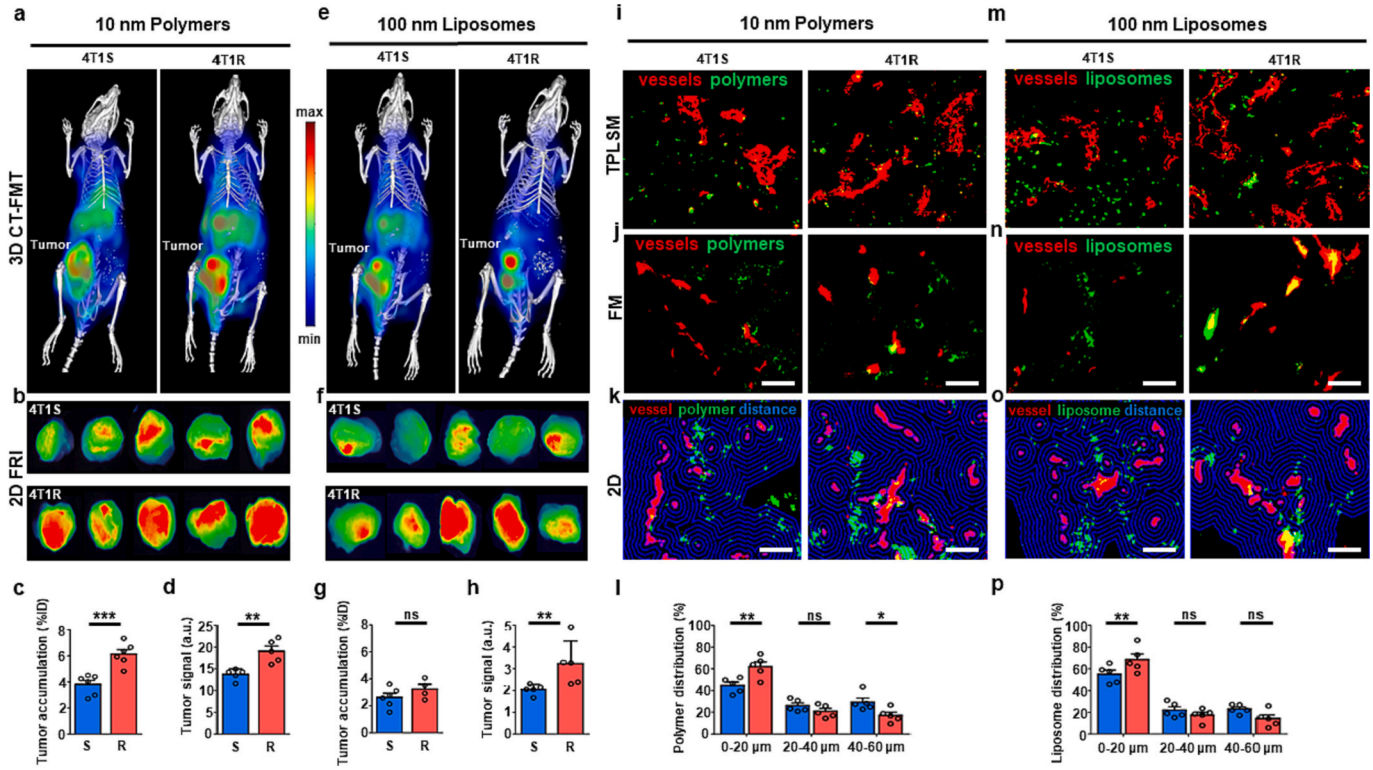

Fig. 5. Nanocarrier accumulation and penetration in 4T1S vs. 4T1R tumors. a-h: In vivo μCT-FMT and ex vivo FRI as well as quantification of the tumor accumulation of fluorophore-labeled pHPMA polymer and pegylated liposomal nanocarriers. At the macroscopic whole tumor level, the accumulation of both nanocarrier materials appeared to be approved, but this was only found to be significant for pHPMA polymers. i-p: At the microscopic and individual blood vessel level, using 3D TPLSM and 2D fluorescence microscopy, it was observed that 10 nm polymers and 100 nm liposomes were more strongly restrained in the (peri)vascular compartment in 4T1R tumors, i.e., within the first 20 μm away from the blood vessel wall. Perfused tumor blood vessels were stained using rhodamine-lectin (red). Scale bar = 50 μm. * $p < 0.05$, ** $p < 0.001$, *** $p < 0.0001$. (For interpretation of the references to colour in this figure legend, the reader is referred to the web version of this article.)

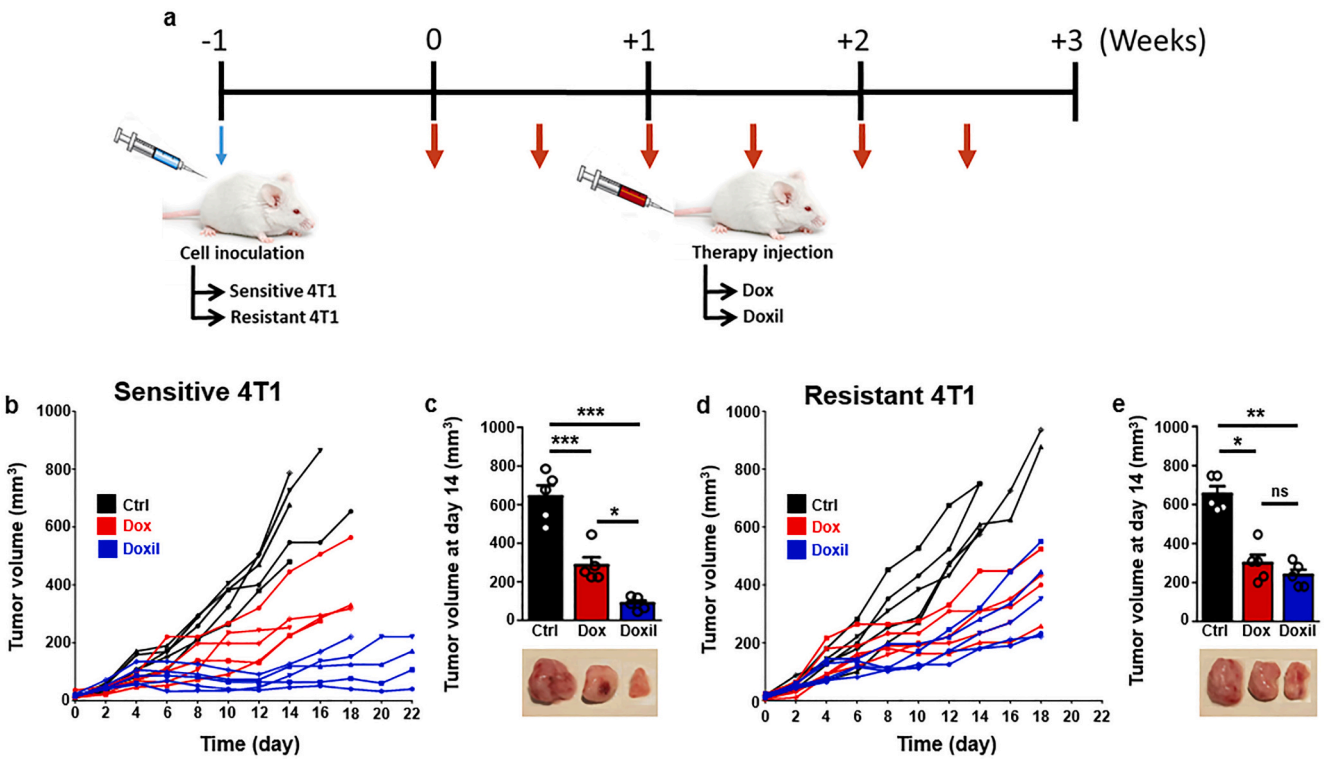

Fig. 6. Nanotherapy treatment outcome is reduced in 4T1R tumors. (a) Study design illustrating that 4T1S and 4T1R tumor-bearing mice were treated six times in three weeks with free and liposomal dox (Doxil). (b-e) Tumor growth curves and tumor volumes at day 14 upon initiation of treatment with free and liposomal dox, indicating that MDR-induced changes in the tumor microenvironment contribute to reduced nanotherapy efficacy. * $p < 0.05$, ** $p < 0.001$, *** $p < 0.0001$.

4T1R tumors. Unexpectedly, treatment with free dox proved equally effective in both 4T1S and 4T1R tumors (Fig. 6b-e), although Pgp expression was significantly higher in 4T1R tumors up to three weeks after in vivo tumor growth (Fig. 4c and d). Doxil treatment was found to be substantially more effective in 4T1S tumors than in 4T1R tumors (Fig. 6b-e). In 4T1R tumors, no therapeutic benefit was observed for doxil treatment over free dox treatment (Fig. 6d and e). This poor response of 4T1R tumors to doxil treatment can likely be attributed to the more stromal microenvironment in resistant tumors, which hinders nanomedicine penetration and distribution (Fig. 5l and p). It cannot be explained on the basis of cellular MDR, since nanomedicine formulations are generally considered to be more efficient in resistant cells as compared to free drugs, as they can bypass drug efflux pumps via their endocytotic internalization [42,43].

Our findings suggest that besides resistance at the cellular level, TME reprogramming by MDR cells is another pathophysiological phenomenon that limits therapeutic outcomes. Thus, theoretically approaching and pharmacologically addressing drug resistance more holistically seems to be needed to achieve better (nano)chemotherapeutic treatment outcomes. An example of such a strategy was reported by Zhang and colleagues, who showed that nanomedicine accumulation occurs even in sensitive 4T1 tumors that suffer from a fairly dense ECM. They employed losartan, which modulates the ECM via inhibition of TGF-β signaling in cancer-associated fibroblasts and reduction of Col-1 deposition, to improve the accumulation and antitumor efficacy of paclitaxel-loaded liposomes [44]. Along the same line of thinking, Murphy and colleagues conducted a clinical trial in patients suffering from pancreatic ductal adenocarcinoma, and showed that adding losartan to neoadjuvant FOLFIRINOX (fluorouracil, leucovorin, oxaliplatin, and irinotecan) improves responses to chemoradiotherapy [45]. Similar ECM-modifying priming treatments appear to be of interest for promoting treatment efficacy in patients with MDR tumors.

4. Conclusions

We show that MDR is a complex pathophysiological phenomenon that extends beyond the cellular level, modulating the microenvironment in tumors and affecting tumor-targeted drug delivery. We exemplified this in the extensively used 4T1 murine TNBC model, showing that resistant 4T1 cells obtain a more mesenchymal phenotype, with upregulation of fibrotic genes, contributing to an MDR phenotype at the TME level. In 3D tumor spheroids and in tumors in vivo, resistant 4T1 cells produced increased amounts of ECM. The latter resulted in decreased penetration of polymers and liposomes out of the blood vessels into the tumor interstitium. Stromal enrichment and reduced penetration hindered tumor-targeted therapy with liposomal dox. Our results indicate that MDR should be addressed both at the cellular and at the TME level.

Author contributions

TL conceived and coordinated the project. OT and TL designed experiments. OT, ASE, KB and SM performed the experiments and analyzed the data. ER, MW, DM and SVS assisted in in vivo and ex vivo imaging. RP, MP and TE synthesized and characterized polymeric nanocarriers. FK contributed imaging expertise. RW and SM coordinated signaling studies. OT, ASE and KB drafted the manuscript. ER, MW, DM, RP, MP, TE, SVS, FK, RW, SM and TL reviewed and edited the manuscript. All authors approved final submission.

Data availability

Data will be made available on request.

Acknowledgements

This work was supported by the German Academic Exchange Service

(DAAD: 57048249), the German Egyptian Research Long-term Scholarship Program (GERLS: 57311832), the European Research Council (ERC-CoG: Meta-Targeting 864121), and the German Research Foundation (DFG: SFB1066 and GRK2375 (Project number: 331065168)). The authors acknowledge assistance from Dr. Sophia Villwock and Dr. Matthias Bartneck for help with animal experiments, microscopy and heat map analysis, and they furthermore thank Dr. Benjamin Theek for providing input on nanocarrier penetration analysis with Definiens® Developer XD 2.0.4. Active support by the Two-Photon Imaging Core Facility at the Interdisciplinary Center for Clinical Research (IZKF) at the Faculty of Medicine at RWTH Aachen University is also gratefully acknowledged.

Appendix A. Supplementary data

Supplementary data to this article can be found online at https://doi.org/10.1016/j.jconrel.2022.12.056.

References

[1] T. Shibue, R.A. Weinberg, EMT, CSCs, and drug resistance: the mechanistic link and clinical implications, nature reviews, Clin. Oncol. 14 (2017) 611–629.
[2] M.M. Gottesman, T. Fojo, S.E. Bates, Multidrug resistance in cancer: role of ATP–dependent transporters, Nat. Rev. Cancer 2 (2002) 48–58.
[3] R.W. Robey, K.M. Pluchino, M.D. Hall, A.T. Fojo, S.E. Bates, M.M. Gottesman, Revisiting the role of ABC transporters in multidrug-resistant cancer, Nat. Rev. Cancer 18 (2018) 452–464.
[4] S.V. Ambudkar, C. Kimchi-Sarfaty, Z.E. Sauna, M.M. Gottesman, P-glycoprotein: from genomics to mechanism, Oncogene 22 (2003) 7468–7485.
[5] A.K. Iyer, A. Singh, S. Ganta, M.M. Amiji, Role of integrated cancer nanomedicine in overcoming drug resistance, Adv. Drug Deliv. Rev. 65 (2013) 1784–1802.
[6] M.E. Davis, Z.G. Chen, D.M. Shin, Nanoparticle therapeutics: an emerging treatment modality for cancer, Nat. Rev. Drug Discov. 7 (2008) 771–782.
[7] T. Lammers, F. Kiessling, W.E. Hennink, G. Storm, Drug targeting to tumors: principles, pitfalls and (pre-) clinical progress, J. Control. Release 161 (2012) 175–187.
[8] R. Pattanshetty, M.S. Rao, Cancer-related fibrosis: prevention or treatment?–A descriptive review, J. Dr. NTR Univ. Health Sci. 10 (2021) 222.
[9] M.P. Czubryt, Common threads in cardiac fibrosis, infarct scar formation, and wound healing, Fibrogenesis Tissue Repair 5 (2012) 1–11.
[10] L.A. Murtha, M.J. Schuliga, N.S. Mabotuwana, S.A. Hardy, D.W. Waters, J. K. Burgess, D.A. Knight, A.J. Boyle, The processes and mechanisms of cardiac and pulmonary fibrosis, Front. Physiol. 8 (2017) 777.
[11] R. Januchowski, P. Zawierucha, M. Ruciński, M. Nowicki, M. Zabel, Extracellular matrix proteins expression profiling in chemoresistant variants of the A2780 ovarian cancer cell line, Biomed. Res. Int. (2014) 2314–6133.
[12] D.A. Senthebane, A. Rowe, N.E. Thomford, H. Shipanga, D. Munro, M.A. Al Mazeedi, H.A. Almazyadi, K. Kallmeyer, C. Dandara, M.S. Pepper, The role of tumor microenvironment in chemoresistance: to survive, keep your enemies closer, Int. J. Mol. Sci. 18 (2017) 1586.
[13] B. Theek, M. Baues, F. Gremse, R. Pola, M. Pechar, I. Negwer, K. Koynov, B. Weber, M. Barz, W. Jahnen-Dechent, Histidine-rich glycoprotein-induced vascular normalization improves EPR-mediated drug targeting to and into tumors, J. Control. Release 282 (2018) 25–34.
[14] C. Ergen, F. Heymann, F. Gremse, M. Bartneck, U. Panzer, R. Pola, M. Pechar, G. Storm, N. Mohr, M. Barz, Targeting distinct myeloid cell populations in vivo using polymers, liposomes and microbubbles, Biomaterials 114 (2017) 106–120.
[15] M. Doube, M.M. Kłosowski, I. Arganda-Carreras, F.P. Cordelières, R.P. Dougherty, J.S. Jackson, B. Schmid, J.R. Hutchinson, S.J. Shefelbine, BoneJ: free and extensible bone image analysis in ImageJ, Bone 47 (2010) 1076–1079.
[16] J. Schindelin, I. Arganda-Carreras, E. Frise, V. Kaynig, M. Longair, T. Pietzsch, S. Preibisch, C. Rueden, S. Saalfeld, B. Schmid, Fiji: an open-source platform for biological-image analysis, Nat. Methods 9 (2012) 676–682.
[17] H. Taymaz-Nikerel, M.E. Karabekmez, S. Eraslan, B. Kırdar, Doxorubicin induces an extensive transcriptional and metabolic rewiring in yeast cells, Sci. Rep. 8 (2018) 1–14.
[18] B. Schrörs, S. Boegel, C. Albrecht, T. Bukur, V. Bukur, C. Holtsträter, C. Ritzel, K. Manninen, A.D. Tadmor, M. Vormehr, Multi-omics characterization of the 4T1 murine mammary gland tumor model, Front. Oncol. 10 (2020) 1195.
[19] L. Gibalová, M. Šereš, A. Rusnák, P. Ditte, M. Labudová, B. Uhrík, J. Pastorek, J. Sedlák, A. Breier, Z. Sulová, P-glycoprotein depresses cisplatin sensitivity in L1210 cells by inhibiting cisplatin-induced caspase-3 activation, Toxicol. in Vitro 26 (2012) 435–444.
[20] F. Li, X. Zhou, H. Zhou, J. Jia, L. Li, S. Zhai, B. Yan, Reducing both Pgp overexpression and drug efflux with anti-cancer gold-paclitaxel nanoconjugates, PLoS One 11 (2016) 1932–6203.
[21] C. Karthika, R. Sureshkumar, M. Zehravi, R. Akter, F. Ali, S. Ramproshad, B. Mondal, P. Tagde, Z. Ahmed, F.S. Khan, Multidrug resistance of Cancer cells and the vital role of P-glycoprotein, Life 12 (2022) 897.
[22] O. Tezcan, U. Gündüz, Vimentin silencing effect on invasive and migration characteristics of doxorubicin resistant MCF-7 cells, Biomed. Pharmacother. 68 (2014) 357–364.
[23] B. Sarkadi, L. Homolya, G. Szakács, A. Váradi, Human multidrug resistance ABCB and ABCG transporters: participation in a chemoimmunity defense system, Physiol. Rev. 86 (2006) 1179–1236.
[24] G. Szakács, J.K. Paterson, J.A. Ludwig, C. Booth-Genthe, M.M. Gottesman, Targeting multidrug resistance in cancer, Nat. Rev. Drug Discov. 5 (2006) 219–234.
[25] J. Shi, W. Liu, Y. Fu, N. Yin, H. Zhang, J. Chang, Z. Zhang, "US-detonated nano bombs" facilitate targeting treatment of resistant breast cancer, J. Control. Release 274 (2018) 9–23.
[26] J. Liu, C. Zhu, L. Xu, D. Wang, W. Liu, K. Zhang, Z. Zhang, J. Shi, Nanoenabled intracellular calcium bursting for safe and efficient reversal of drug resistance in tumor cells, Nano Lett. 20 (2020) 8102–8111.
[27] C.L. Sommers, S.W. Byers, E.W. Thompson, J.A. Torri, E.P. Gelmann, Differentiation state and invasiveness of human breast cancer cell lines, Breast Cancer Res. Treat. 31 (1994) 325–335.
[28] Ö.D. Işeri, M.D. Kars, F. Arpaci, C. Atalay, I. Pak, U. Gündüz, Drug resistant MCF-7 cells exhibit epithelial-mesenchymal transition gene expression pattern, Biomed. Pharmacother. 65 (2011) 40–45.
[29] A.M. Haslehurst, M. Koti, M. Dharsee, P. Nuin, K. Evans, J. Geraci, T. Childs, J. Chen, J. Li, J. Weberpals, EMT transcription factors snail and slug directly contribute to cisplatin resistance in ovarian cancer, BMC Cancer 12 (2012) 1–10.
[30] Q.-Q. Li, J.-D. Xu, W.-J. Wang, X.-X. Cao, Q. Chen, F. Tang, Z.-Q. Chen, X.-P. Liu, Z.-D. Xu, Twist1-mediated adriamycin-induced epithelial-mesenchymal transition relates to multidrug resistance and invasive potential in breast cancer cells, Clin. Cancer Res. 15 (2009) 2657–2665.
[31] C. Zeltz, I. Primac, P. Erusappan, J. Alam, A. Noel, D. Gullberg, Cancer-associated fibroblasts in desmoplastic tumors: Emerging role of integrins, in: Seminars in cancer Biology, Elsevier, 2020, pp. 166–181.
[32] R. Rimal, P. Desai, R. Daware, A. Hosseinnejad, J. Prakash, T. Lammers, S. Singh, Cancer-associated fibroblasts: origin, function, imaging, and therapeutic targeting, Adv. Drug Deliv. Rev. (2022) 114504.
[33] A.N. Shah, J.M. Summy, J. Zhang, S.I. Park, N.U. Parikh, G.E. Gallick, Development and characterization of gemcitabine-resistant pancreatic tumor cells, Ann. Surg. Oncol. 14 (2007) 3629–3637.
[34] A.D. Yang, F. Fan, E.R. Camp, G. van Buren, W. Liu, R. Somcio, M.J. Gray, H. Cheng, P.M. Hoff, L.M. Ellis, Chronic oxaliplatin resistance induces epithelial-to-mesenchymal transition in colorectal cancer cell lines, Clin. Cancer Res. 12 (2006) 4147–4153.
[35] G. Konecny, N. Venkatesan, G. Yang, J. Dering, C. Ginther, R. Finn, M. Rahmeh, M. S. Fejzo, D. Toft, S. Jiang, Activity of lapatinib a novel HER2 and EGFR dual kinase inhibitor in human endometrial cancer cells, Br. J. Cancer 98 (2008) 1076–1084.
[36] G.Z. Cheng, J. Chan, Q. Wang, W. Zhang, C.D. Sun, L.-H. Wang, Twist transcriptionally up-regulates AKT2 in breast cancer cells leading to increased migration, invasion, and resistance to paclitaxel, Cancer Res. 67 (2007) 1979–1987.
[37] H. Kajiyama, K. Shibata, M. Terauchi, M. Yamashita, K. Ino, A. Nawa, F. Kikkawa, Chemoresistance to paclitaxel induces epithelial-mesenchymal transition and enhances metastatic potential for epithelial ovarian carcinoma cells, Int. J. Oncol. 31 (2007) 277–283.
[38] R.C. Stone, I. Pastar, N. Ojeh, V. Chen, S. Liu, K.I. Garzon, M. Tomic-Canic, Epithelial-mesenchymal transition in tissue repair and fibrosis, Cell Tissue Res. 365 (2016) 495–506.
[39] R. Kalluri, E.G. Neilson, Epithelial-mesenchymal transition and its implications for fibrosis, J. Clin. Invest. 112 (2003) 1776–1784.
[40] D.H. Peng, C. Ungewiss, P. Tong, L.A. Byers, J. Wang, J.R. Canales, P.A. Villalobos, N. Uraoka, B. Mino, C. Behrens, ZEB1 induces LOXL2-mediated collagen stabilization and deposition in the extracellular matrix to drive lung cancer invasion and metastasis, Oncogene 36 (2017) 1925–1938.
[41] G.V. Echeverria, Z. Ge, S. Seth, X. Zhang, S. Jeter-Jones, X. Zhou, S. Cai, Y. Tu, A. McCoy, M. Peoples, Resistance to neoadjuvant chemotherapy in triple-negative breast cancer mediated by a reversible drug-tolerant state, Sci. Transl. Med. 11 (2019) 1946–6234.
[42] O. Tezcan, T. Ojha, G. Storm, F. Kiessling, T. Lammers, Targeting cellular and microenvironmental multidrug resistance, Expert Opin. Drug Deliv. 13 (2016) 1199–1202.
[43] Z. Gao, L. Zhang, Y. Sun, Nanotechnology applied to overcome tumor drug resistance, J. Control. Release 162 (2012) 45–55.
[44] L. Zhang, Y. Wang, Y. Yang, Y. Liu, S. Ruan, Q. Zhang, X. Tai, J. Chen, T. Xia, Y. Qiu, High tumor penetration of paclitaxel loaded pH sensitive cleavable liposomes by depletion of tumor collagen I in breast cancer, ACS Appl. Mater. Interfaces 7 (2015) 9691–9701.
[45] J.E. Murphy, J.Y. Wo, D.P. Ryan, J.W. Clark, W. Jiang, B.Y. Yeap, L.C. Drapek, L. Ly, C.V. Baglini, L.S. Blaszkowsky, Total neoadjuvant therapy with FOLFIRINOX in combination with losartan followed by chemoradiotherapy for locally advanced pancreatic cancer: a phase 2 clinical trial, JAMA Oncol. 5 (2019) 1020–1027.